JOURNAL OF CATALYSIS **150**, 284–300 (1994)

Vanadia–Titania Aerogels

III. Influence of Niobia on Structure and Activity for the Selective Catalytic Reduction of NO by NH_3

M. Schneider,* U. Scharf,† A. Wokaun,† and A. Baiker*[,1]

*Department of Chemical Engineering and Industrial Chemistry, Swiss Federal Institute of Technology, ETH-Zentrum, CH-8092 Zürich, Switzerland; and †Physical Chemistry II, University of Bayreuth, D-95440 Bayreuth, Germany

Received March 11, 1994; revised June 27, 1994

Niobia-doped vanadia–titania aerogels with 20 wt% nominal "V_2O_5" and 2–6 wt% nominal "Nb_2O_5" have been prepared by a two-stage sol–gel process with subsequent supercritical drying. A titania gel was synthesized by the addition of an acidic hydrolysant to tetrabutoxytitanium(IV) in methanol. The methanolic, premixed solution of niobium(V) pentaethoxide and vanadium(V) oxide tri-*n*-propoxide was added after redispersing the titania gel. The influence of niobia loading on the morphological and chemical properties of the aerogels was studied. Similarly a ternary xerogel (20 wt% V_2O_5, 6 wt% Nb_2O_5) was prepared for comparison with the corresponding aerogel. The aero(xero-)gels were characterized by means of N_2 physisorption, X-ray diffraction, thermal analysis coupled with mass spectrometry, scanning electron microscopy, and vibrational spectroscopy. The meso- to macroporous aerogels possess BET surface areas of 176–203 $m^2\,g^{-1}$ after calcination at temperatures $\leq$673 K and contain well-developed anatase crystallites of 7–8 nm mean size. For the calcination at 723 K niobia is suggested to retard both crystallization of the vanadia phase and phase transformation of anatase to rutile. The corresponding BET surface area is 114 $m^2\,g^{-1}$. In contrast, the xerogel calcined at 673 K is micro- to mesoporous, possesses a BET surface area of 117 $m^2\,g^{-1}$, and contains anatase as well as monoclinic TiO_2 with mean crystallite sizes of 11 and 15 nm, respectively. Crystalline V_2O_5 was only detected for the xerogel calcined at 773 K. In all other samples the vanadia phase consists of highly dispersed vanadium oxo clusters together with more extended structures, especially at temperatures $\geq$673 K. The catalytic properties of the aero(xero-)gels were tested with the selective catalytic reduction of NO by NH_3. The variation of the niobia loading from 2 to 6 wt% Nb_2O_5 did not affect the activity. An increase of the calcination temperature from 573 to 723 K led to a significant activity rise of the aerogel catalysts. The xerogel calcined at 673 K exhibited the highest activity among all catalysts tested.

INTRODUCTION

Our previous studies (1, 2) demonstrated that highly dispersed vanadia–titania aerogels with loadings up to 30 wt% nominal "V_2O_5" can be synthesized by high-temperature supercritical drying. These binary aerogels reached activities for the selective catalytic reduction (SCR) of NO by NH_3, which were as high as that of multiply grafted vanadia on titania catalysts (3).

In view of its environmental importance, the selective catalytic reduction of NO by NH_3 has been studied intensively, and various reaction mechanisms have been proposed (4). There is an ongoing debate about the active site in the SCR reaction (5–11). In our recently published DRIFT studies on vanadia–titania aerogels with 20 wt% V_2O_5 (12), we could show that Brønsted-bound ammonia is involved in the SCR reaction. Moreover, the SCR activities correlate with the fraction of Brønsted-bound ammonia, which significantly increases with the vanadia loading of the aerogels.

Hydrated niobium oxide is known to be an alternative solid acid and has been found active in many acid-catalyzed reactions (13, 14). The preparation as well as the acidic properties of niobia and niobia-containing mixed aerogels, prepared by the metal alkoxide sol–gel route, have recently been described by Maurer *et al.* (15–17). The authors revealed an interesting relationship between molecular structure, stability, and acidity (15, 17). In conjunction with titania, niobia addition was found to generate additional acidic sites below a pK_a value of 3.3, which was the lowest acidity value determined for a titania aerogel (17). The Brønsted acidic sites were active in the catalytic isomerization of 1-butene. However, the effectiveness of niobia was lost at high temperatures due to

---

[1] To whom correspondence should be addressed.

0021-9517/94 $6.00

the formation of Nb_2TiO_7 (≥ca. 1073 K). Datka *et al.* (18) prepared niobia supported on TiO_2 (Degussa P25) by incipient wetness. At 623 K the authors did not find any acidity-increasing effect on Lewis or Brønsted acidic sites due to the presence of niobia on TiO_2. In contrast to this result, Okazaki and Okuyama (19) showed that at low Nb : Ti atomic ratio the impregnated niobia/titania (surface oxide) is more active than the coprecipitated oxide (mixed oxide) in the isomerization of cyclopropane at 523 K. The authors ascribed this difference to the higher Brønsted acidity when niobia is impregnated onto titania. Their main interest, however, was centered on the investigation of coprecipitated niobia–titania catalysts and niobia impregnated on different supports for SCR of NO by NH_3 (19). The catalytic activity of niobia supported on titania was much higher than that of niobia supported on alumina, zirconia, or silica (in decreasing order). It reached 80–90% conversion at temperatures ≥723 K. When compared to the catalytic activities of vanadia–titania, that of niobia–titania was still lower, especially at temperatures lower than 573 K. This behavior was attributed to the lower redox functionality of niobia (reduction of Nb_2O_5 to NbO_2 in H_2 at 1273–1473 K), although it possessed a considerable amount of Brønsted acidic sites.

To our knowledge, the direct preparation of niobia-containing vanadia–titania aerogels has not been reported thus far. The coupling of the solution–sol–gel process (SSG) (20) with supercritical drying (SCD) (21) offers the combination of the intrinsic advantages of the SSG method (dispersion, homogeneity, molecular mixing) with the favorable textural characteristics of aerogels (22–24). Altogether it prompted us to investigate the interaction of our recently described active vanadia–titania aerogels (1, 2) with the favorable acidic properties of niobium oxide-containing materials (13, 14).

Here we report the direct preparation and characterization of niobia-containing vanadia–titania aerogels. The influence of different niobia contents as well as calcination temperature on the structural and chemical properties of aerogels with constant 20 wt% V_2O_5 was investigated. Furthermore, a comparison between ternary aerogel and xerogel is given and their catalytic performance in the SCR of NO by NH_3 was tested.

EXPERIMENTAL

Synthesis

Throughout the article a set of acronyms for the individual aerogels is used. Taking V20Nb6 as an example, "Vnn" designates the nominal vanadia content of 20 wt% V_2O_5. "Nbn" stands for the nominal niobia content of 6 wt% Nb_2O_5. V20Nb6*X* designates the related xerogel. Correspondingly, Nb6 denotes the binary niobia–titania aerogel.

Analytical-grade reagents were used throughout this work. The preparation of the niobia-containing aerogels followed closely the one of the binary aerogel V20NP10 in Ref. (1). Consequently only a short description will be given here. The solution–sol–gel process was carried out in an antiadhesive, closed Teflon beaker, under nitrogen atmosphere and at ambient temperature (297 ± 2 K). The acidic hydrolysant diluted with methanol was added to a methanolic solution of tetrabutoxytitanium(IV) (TBOT), which contained 32.0 g TBOT in all preparations. The resulting titania gels were aged 4 h and then redispersed with different amounts of added methanol (Table 1). Prior to addition, pentaethoxyniobium (PEON) and vanadium oxide tri-*n*-propoxide (VOTP) were premixed in a dry glove box for 3.5 h, diluted with methanol (Table 1), and transferred into the nonviscous titania solution by syringe. After a second aging step of additional 4 h under vigorous stirring (ca. 1000 rpm), the appropriate amount of doubly distilled water diluted in methanol (Table 1) was introduced in the same way, so as to adjust the stoichiometric hydrolysis level. The translucent solution was stirred vigorously for another 15 h.

The resulting sol–gel product was transferred in a stainless-steel liner into an autoclave with a net volume of 1.09 liters. The total volume of methanol amounted to ca. 245 ml in all cases. The corresponding critical data for methanol, as the dominating component of all SSG solvents used here, are V_c = 118 ml mol^{-1}, T_c = 513 K, and p_c = 8.1 MPa (25). The supercritical drying was performed in a batch operation and the appropriate conditions were set as follows: nitrogen prepressure 10 MPa, heating rate of 1 K min^{-1} to 533 K, 30 min thermal equilibration (final pressure ca. 25 MPa), and isothermal depressurization at 0.1 MPa min^{-1} (1). With the vanadia-containing aerogels violet clumps and powder formed, in the case of Nb6 (niobia–titania aerogel) white clumps and powder. These brittle aerogel grains were ground in a mortar. Finally, portions of the uncalcined (raw) aerogel powder were calcined in a tubular reactor with upward flow. The temperatures given corresponded to the oven temperature. GHSV amounted to ca. 1000 h^{-1} (ca. 3 g aerogel sample). To remove most of the organic residues under mildly oxidative conditions, all aerogel samples were first heated at 2.5 K min^{-1} in a flow of 0.35 liters min^{-1} nitrogen and 0.15 liters min^{-1} air to 573 K and held for 1 h. After being cooled to ca. 353 K in the diluted air flow and heated at 5 K min^{-1}, this time in air flowing at 0.5 liters min^{-1}, the portions of the raw aerogels were calcined for another 5 h at 573 K. Two samples of V20Nb6 were calcined at 673 and 723 K, respectively.

With V20Nb6*X* (X for xerogel) the wet-chemical synthesis followed the above-described procedure for

TABLE 1

Changes of the Preparation Conditions for Varying the Niobia Loading

Aerogel	Methanol used for redispersion (ml)[a]	VOTP (g) and PEON (g) in methanol (ml)[b]			Hydrolysant: H_2O (ml) in methanol (ml)[c]	
Nb6	90	0	1.15	3.7	0.325	1.3
V20Nb2	70	5.12	0.46	20	1.25	5
V20Nb4	68	5.26	0.95	22	1.38	5
V20Nb6 (V20Nb6X)	65	5.41	1.46	24	1.52	6

[a] Amount of methanol used for redispersion of the titania gel.

[b] Composition of precursor solution: vanadium(V) oxide tri-*n*-propoxide (VOTP), pentaethoxyniobium(V) (PEON).

[c] Composition of the hydrolysant "completing" the stoichiometric hydrolysis of VOTP and PEON.

V20Nb6 (Table 1), with the following exceptions. After the addition of the hydrolysant for the "completion" of stoichiometric hydrolysis the ternary sol was kept under a nitrogen flow of 0.12 liters min^{-1} for 87 h. The resulting viscous sol–gel product was transferred into a vacuum oven and dried stepwise (293 K, 10 kPa, 9 h; 313 K, 10 kPa, 62 h; and 373 K, 8 kPa, 9 h). The soft xerogel clumps were ground in a mortar. Then the xerogel powder was dried in the tubular reactor at 373 K for another 72 h under a nitrogen flow of 0.25 liters min^{-1}. This procedure led to a brown dense powder. Finally, portions of the raw xerogel powder were calcined in the tubular reactor. GHSV was ca. 6000 h^{-1} (ca. 3 g xerogel sample). All xerogel samples were oxidatively treated in a flow of 0.35 liters min^{-1} nitrogen and 0.15 liters min^{-1} air at 573 K for 1 h. After being cooled to ca. 353 K in the same flow and heated again at 5 K min^{-1}, this time in air flowing at 0.5 liters min^{-1}, two portions of the raw xerogels were calcined for another 5 h at 573 and 673 K, respectively. With a third sample the calcination in flowing air was carried out in two steps. After holding the temperature at 673 K for 1 h, the xerogel portion was heated at 2.5 K min^{-1} to 773 K and held at this temperature for 4 h. Surprisingly, the higher the calcination temperature the darker the color became.

Loadings are expressed in weight percent of nominal vanadium(V) pentoxide (V_2O_5) as well as niobium pentoxide (Nb_2O_5) throughout the text. They are generally calculated on the basis of the weighed amounts (Table 1). The vanadium contents were independently confirmed by thermal gravimetry (oxidation–reduction cycles).

Physicochemical Characterization

The specific surface areas (S_{BET}), mean cylindrical pore diameters ($\langle d_p \rangle$), and specific adsorption pore volumes (V_{pN_2}) were obtained from N_2 physisorption at 77 K using a Micromeritics ASAP 2000 instrument. Prior to measurement, the samples were degassed to 0.1 Pa at 423 K (523 K, with V20Nb6X calcined at 673 K). S_{BET} were calculated in a relative pressure range between 0.05 and 0.2 assuming a cross-sectional area of 0.162 nm^2 for the N_2 molecule. The pore size distributions were calculated applying the Barrett–Joyner–Halenda (BJH) method (26) to the desorption (aerogels with type-H1 hysteresis (27)) or adsorption (xerogels with type-H2 hysteresis (27)) branches of the isotherms (28). The assessments of microporosity were made from *t*-plot constructions ($0.3 < t < 0.5$ nm, aerogels; $0.7 < t < 0.9$ nm, xerogels), using the Harkins–Jura correlation (29).

X-ray powder diffraction (XRD) patterms were measured on a Siemens Θ/Θ D5000 powder X-ray diffractometer. The diffractograms were recorded with Cu*Kα* radiation over a 2Θ range of 10–80° and a position-sensitive detector with Ni filter. The mean crystallite sizes were determined from the Scherrer equation (30) and the (200) or (101) reflection (only in the presence of crystalline V_2O_5) for anatase (31), the (110) reflection for rutile (32) as well as the (002) reflection for monoclinic TiO_2 (33).

TG and DTA investigations were performed on a Netzsch STA 409 instrument coupled with a Balzers QMG 420/QMA 125 quadrupole mass spectrometer, equipped with Pt–Rh thermocouples and Pt crucibles. A heating rate of 10 K min^{-1} and an air flow of 25 ml min^{-1} were used. The weight of both the samples and the α-Al_2O_3 reference was ca. 50 mg. Total carbon and hydrogen contents were determined with a LECO CHN-900 elemental microanalysis apparatus.

Scanning electron micrographs were recorded on a JEOL instrument (Model JSM-840 A) with a 20 keV electron beam. The oxide powders were spread on adhesive conducting carbon tapes (Leit-Tab) and overcorated with gold.

Prior to the Raman measurement, samples were dried at 393 K, transferred to 3-mm-diameter test tubes under argon, and sealed to prevent rehydration. Spectra were excited using the 530.8-nm line of a krypton ion laser (Coherent, model Innova 300). 20 mW of power were focused onto a spot of 0.1 mm diameter on the sample. For detection a triple spectrograph combined with a cooled intensified multichannel detection system was used, which has been described elsewhere (34). Resolution was set at 5–6 cm^{-1}. Typically, the integration time corresponded to 100 s, and 10 data sets were coadded.

Diffuse reflectance IR measurements were recorded on an FTIR instrument (Digilab, Model FTS 80) equipped with an "environmental chamber" placed into a diffuse reflectance accessory (Spectra-Tech). Samples were pretreated by heating to 473 K under a flow of dried oxygen (removal of physisorbed water), and were subsequently cooled to 298 K prior to the measurements. The sample cell was purged with a small flow of oxygen during the measurements. A total of 512 scans were accumulated for each spectrum, at a resolution of 2 cm^{-1}.

Selective Catalytic Reduction of NO by NH_3

The continuous microreactor, the experimental procedure, and the analysis of the gases were described in detail in Part I (1). The simulated stack emission feed comprised 900 vppm NO and NH_3, 1.8 v% O_2, with argon being the balance gas.

The catalytic testing of the agglomerated aerogels followed the procedure reported in Ref. (1). In brief, the reactor bed consisted of 44-mg granules (120–300 μm), corresponding to a bed volume of 0.126 cm^3 and bed height of 1 cm. With xerogel V20Nb6X calcined at 673 K, the xerogel powder was agglomerated at 20 MPa for 1 min. The reactor bed was made up of 112 mg catalyst with a bed volume of 0.089 cm^3. The differential reactor test was carried out between 360 and 405 K and space velocities of 24000–142000 h^{-1} (STP; 273.15 K, 1 atm), otherwise as mentioned in Ref. (1).

Preliminary tests with different granule fractions in Ref. (1) showed that the kinetic data determined below 440 K were independent of the particle size (<500 μm), indicating that internal mass transfer influences could be ruled out. The experimental error of the catalytic testing was less than 10%. The error of the apparent activation energies derived by linear regression of the corresponding Arrhenius plots was less than 3%.

RESULTS

Properties of both the calcined aerogel catalysts and their parent raw aerogels are listed in Table 2. The data of V20NP10 from Ref. (1) are quoted for comparison.

Physicochemical Characterization

Nitrogen physisorption. The adsorption/desorption isotherms and the differential pore size distribution derived from the desorption branch (28) for a sample of V20Nb6 calcined at 673 K in air are depicted in Fig. 1, as representatives of all aerogels calcined at temperatures ≤723 K. They show a type-IV isotherm with a type-H1 desorption hysteresis according to IUPAC classification (27) and meso- to macroporosity with little microporosity. The specific micropore surface areas, estimated from the corresponding *t*-plot analysis, are ≤13 $m^2\ g^{-1}$. The specific surface areas (S_{BET}) range from 176 to 203 $m^2\ g^{-1}$, and the specific nitrogen pore volumes (V_{pN_2}) range from 0.90 to 1.01 $cm^3\ g^{-1}$. The very broad, asymmetric pore-size distributions (Fig. 1) also emerge from the comparison of the pore size maxima (ca. 50 nm, Fig. 1) with the mean cylindrical pore sizes $\langle d_p \rangle$ given in Table 2. The V20Nb6 sample calcined at 723 K shows a significant decrease of the S_{BET} to 114 $m^2\ g^{-1}$ with a virtually unaltered V_{pN_2} of 0.95 $cm^3\ g^{-1}$, which is consistent with the decreased contribution of pores ≤ca. 5 nm.

Calcination of a portion of xerogel V20Nb6*X* at 573 K did not result in reliable N_2-physisorption analysis (see thermal analysis studies below). Figure 2 depicts the adsorption/desorption isotherms and the differential pore size distribution derived from the adsorption branch (28) for the xerogel sample V20Nb6*X* calcined at 673 K. It shows a type I-IV isotherm with a type-H2 desorption hysteresis (27), which results in a micro- to mesoporous pore-size distribution with a pore size maximum at ca. 3 nm (Fig. 2, Table 2). The specific micropore surface area estimated to 113 $m^2\ g^{-1}$ (from *t*-plot analysis) indicates that the micropores contribute most to the BET surface area of 117 $m^2\ g^{-1}$. The calcination at 773 K caused virtually an elimination of the microporosity, which resulted in an S_{BET} of 10 $m^2\ g^{-1}$, a mesoporous symmetric pore size distribution with a maximum at ca. 24 nm, and a consequently virtually unchanged specific pore volume (Table 2). Moreover, the V20Nb6*X* sample calcined at 773 K showed a type-IV isotherm with type-H1 desorption hysteresis.

X-ray diffraction. The niobia-containing aerogels, whether raw or calcined at 573–673 K, contain well-developed anatase crystallites (31) of 6.3–7.9 nm and 6.5–8.2 nm mean size, respectively (Table 2). Calcination generally caused an increase of the mean crystallite size, often lying within the precision of the line-broadening analysis. Furthermore, Table 2 indicates that both the vanadia and niobia phase are X-ray amorphous.

The XRD patterns of the V20Nb6 series, both raw and after calcination at 673 and 723 K, are depicted in Fig. 3. It is evident that up to 723 K the crystallinity of anatase increased, resulting in a mean crystallite size of 10 nm (Table 2, Fig. 3). However, vanadia as well as niobia remained X-ray amorphous even during calcination at 723 K.

Figure 4 shows the XRD patterns of the xerogel series

TABLE 2

Morphological Properties of the Aero(Xero-)Gel Catalysts Calcined in Flowing Air at Different Temperatures

Aerogel	Calcination (K)	S_{BET} (S_t)[a] (m^2/g)	$\langle d_p \rangle$ (nm)[b]	V_{pN_2} (cm^3/g)	XRD crystallinity and $\langle d_c \rangle$ (nm)[c]		
V20*NP*10[d]	573	220(12)	20	1.11	A	6.5	(6.3)
Nb6	573	190 (12)	21	1.01	A	8.2	(7.9)
V20Nb2	573	203 (11)	18	0.90	A	7.0	(6.5)
V20Nb4	573	193 (13)	19	0.91	A	7.2	(7.1)
V20Nb6	573	194 (9)	20	0.97	A	7.3	(7.2)
V20Nb6	673	176 (8)	22	0.98	A	7.5	(7.2)
V20Nb6	723	114 (8)	33	0.95	A	10	(7.2)
V20Nb6*X*	573	—[e]	—[e]	—[e]	a	a	(a)
V20Nb6*X*	673	117 (113)	3	0.08	A, T	11, 15	(a)
V20Nb6*X*	773	10 (1)	24	0.06	R, A, S	28, 30, —[e]	(a)

[a] (S_t) in parentheses specific micropore surface area derived from *t*-plot analysis.

[b] $\langle d_p \rangle = 4V_{pN_2}/S_{BET}$.

[c] A (anatase), R (rutile), T (monoclinic TiO_2), S (shcherbinaite, V_2O_5) in order of decreasing intensity, and a (amorphous); $\langle d_c \rangle$ corresponding mean crystallite sizes, in parentheses the values of the raw materials.

[d] From Ref. (1): V20NP10—20 wt% V_2O_5; basic preparation procedure for this work.

[e] —, not determinable with reasonable reliability.

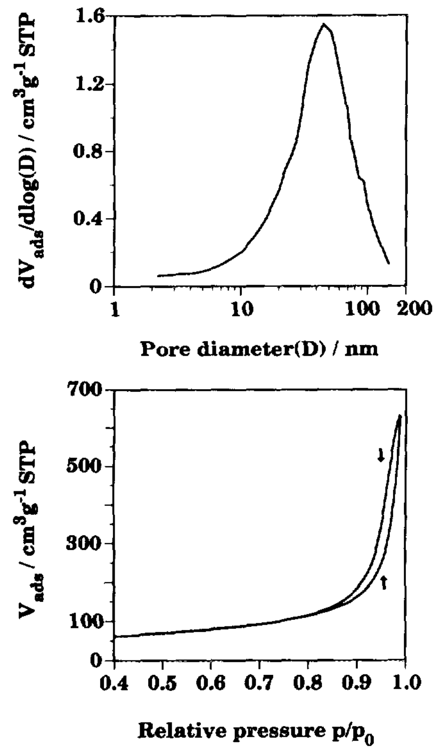

FIG. 1. Nitrogen physisorption on aerogel V20Nb6 calcined at 673 K in air. Bottom, adsorption (↑)/desorption(↓) isotherms (STP; 273.15 K, 1 atm); top, differential pore size distribution derived from the desorption branch of N_2 physisorption. Designations of catalysts are explained under Experimental.

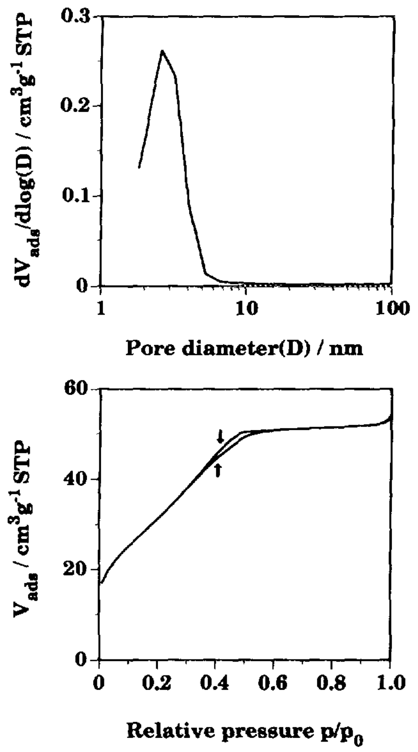

FIG. 2. Nitrogen physisorption on xerogel V20Nb6*X* calcined at 673 K in air. Bottom, adsorption(↑)/desorption(↓) isotherms (STP; 273.15 K, 1 atm); top, differential pore size distribution derived from the adsorption branch of N_2 physisorption.

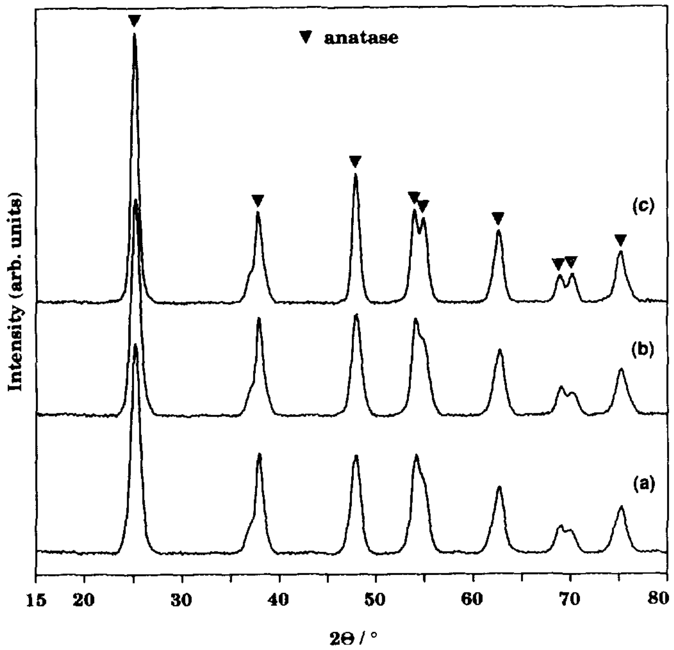

FIG. 3. X-ray diffraction patterns (Cu*K*α) of aerogel V20Nb6 calcined at different temperatures in air: (a) raw, (b) 673 K, (c) 723 K. ▼, anatase. Catalyst designations are explained under Experimental.

V20Nb6*X*, whether raw or calcined at 573, 673, and 773 K. Up to 573 K the xerogel remained X-ray amorphous (patterns (a and b)). However, the calcination at 673 K led to crystalline anatase as well as monoclinic TiO_2 (33). At 773 K crystalline V_2O_5 (shcherbinaite) (35) evolved and concomitantly most of the anatase phase topotactically transformed into rutile (32), resulting in a rutile fraction of ca. 0.86 (36) (Fig. 4, pattern (d)) (1, 36–38). Thus the V20Nb6*X* sample calcined at 773 K consists of highly crystalline rutile, anatase, and shcherbinaite with mean crystallite sizes of 28 and 30 nm, respectively (Table 2). As already mentioned in the physisorption studies above, this crystallization–transformation gave rise to a significant decrease of the BET surface area with concomitant elimination of the microporosity (Table 2).

Thermal analysis. Thermal analysis was performed in flowing air with a heating rate of 10 K min^{-1}. The thermoanalytical results measured for the aerogel sample V20Nb6 calcined at 573 K are depicted in Fig. 5, which is representative of all aerogels calcined up to 673 K. The weight loss originated predominantly from the evolution of water (desorption of physisorbed water, dehydroxylation), which was already present in the aerogels, and from the oxidation of organic residues. This feature emerges from relating the TG curve to the ion intensities of mass/charge ratios (*m*/*z*) corresponding to H_2O and CO_2 (Fig. 5). Consequently, despite the calcination at 573 K for 5 h a detectable amount of organic contaminants persists in the aerogels. These organic residues amount to $\leq$ca. 0.1 wt% carbon, compared to ca. 2 wt% in the raw samples (derived from elemental microanalysis). They originate mainly from the realkoxylation of surface hydroxyl groups during supercritical drying and, probably to a low extent, from some unhydrolyzed incorporated alkoxide ligands. The evolution of H_2O began at room temperature and reached a maximum at 433 K. The CO_2 evolution occurred at ca. 450 K and reached a maximum at 620 K. In accordance with this, the DTA curve shows a broad endothermal signal, which corresponds to desorption of physisorbed H_2O and dehydroxylation (Fig. 5). The exothermal DTA peak at 808 K reflects the crystallization of the vanadia component to V_2O_5. At ca. 670 K the reoxidation of the partly reduced vanadia component, related to the weight uptake in the TG profile, began to dominate over the H_2O- and CO_2 evolution. Considering the greenish color of the aerogel samples after the calcination at 573–673 K and the very poor reducibility of Nb_2O_5, the weight uptake of 0.7 wt% is ascribed to a vanadia component in a still partly reduced state (1). The thermoanalytical investigation of a portion of V20Nb6 calcined at 673 K showed a minor overall weight loss, but similar

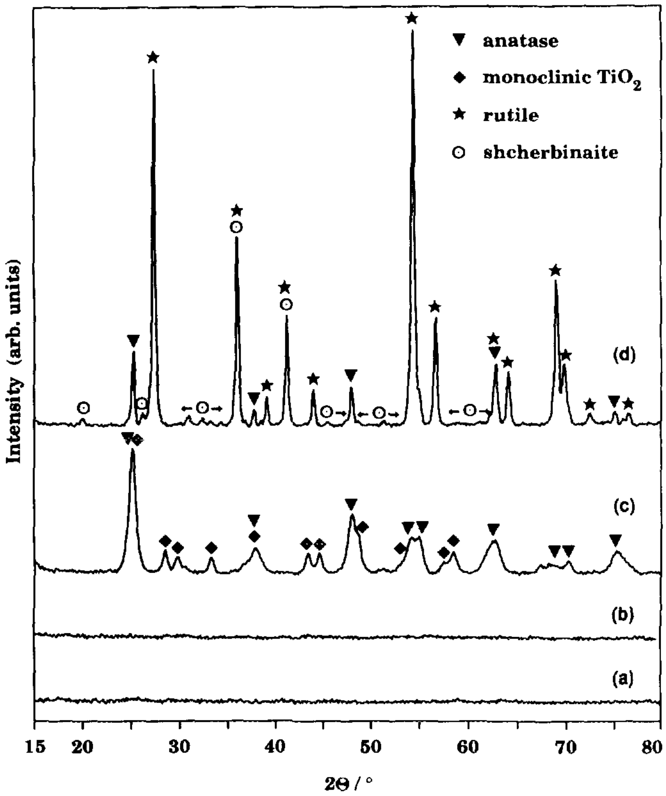

FIG. 4. X-ray diffraction patterns (Cu*K*α) of xerogel V20Nb6*X* calcined at different temperatures in air: (a) raw, (b) 573 K, (c) 673 K, (d) 773 K. ▼, anatase; ◆, monoclinic TiO_2; ★, rutile; and ○, shcherbinaite.

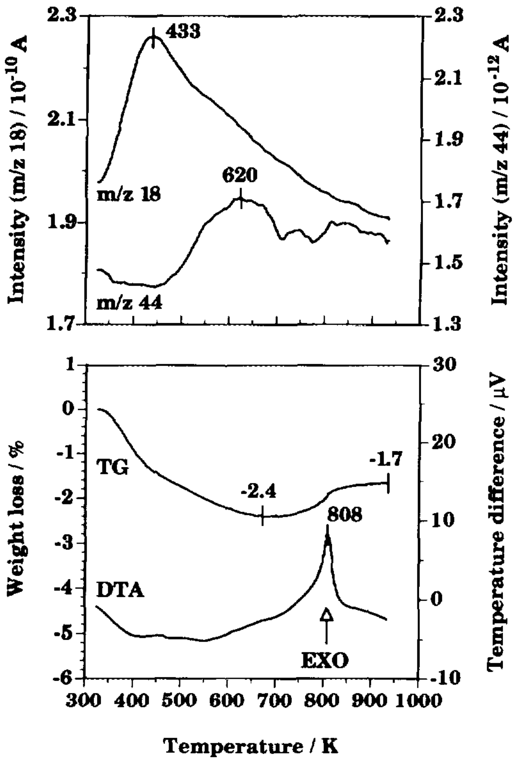

FIG. 5. Thermoanalytical investigation of aerogel V20Nb6 calcined at 573 K. Bottom, TG and DTA curves; top, ion intensities of m/z (CO_2^+) = 44 (CO_2) and $m/z(H_2O^+)$ = 18 (water). Heating rate, 10 K min^{-1}, air flow: 25 ml min^{-1}. Designations of catalysts are explained under Experimental.

weight uptake of 0.7 wt%. This behavior is indicative of a virtually unchanged overall oxidation state of the vanadium component despite the higher calcination temperature of 673 K. The crystallization reached a maximum at 805 K.

The thermoanalytical behavior of the xerogel sample V20Nb6*X* calcined at 673 K is illustrated in Fig. 6. The first evolution of H_2O (physisorbed water, dehydroxylation) appeared at ca. 300 K and attained maximum intensity at 390 K. The second H_2O evolution with a maximum at 790 K originated from the oxidation of organic residues, which is reflected by the trace for m/z = 44 (CO_2) with a maximum at 785 K (Fig. 6). In agreement with this, the DTA curve is dominated by an exothermal signal at 780 K. The endothermal peak at 935 K represents melting of V_2O_5, which is supposed to have crystallized during the exothermal combustion of the organic contaminants. This marked thermal resistance of the organic residues is shown by the carbon contents of the xerogel series V20Nb6*X*, both raw and calcined at 573, 673, and 773 K, amounting to 16.4, 7.8, 1.7, and <0.1 wt% carbon, respectively. Only the calcination at 773 K was efficient in removing most of the organic residues. However, this temperature was too high to avoid crystallization of V_2O_5 and anatase-to-rutile transformation (see XRD studies above, Fig. 4). The thermal resistance of the organic contaminants seems to be based on the above-mentioned microporosity of the V20Nb6*X* sample calcined at 673 K (Fig. 2, Table 2). So the reason for the unreliable N_2-physisorption results of the V20Nb6*X* sample calcined at 573 K is suggested to be occlusion of the internal surface by the considerable amount of organic residues (7.8 wt% carbon), which persists in the xerogel sample even after calcination at 573 K for 5 h.

Scanning electron microscopy. The binary 6 wt% Nb_2O_5–TiO_2 aerogel exhibits an open, unstructured, sponge-like appearance in the scanning electron micrograph (Fig. 7, bottom). The catalyst containing 20 wt% V_2O_5 and 80 wt% TiO_2 (top) appears to consist of more densely packed, patch-like aggregates with a less open surface. The ternary aerogel V20Nb6 calcined at 573 K (Fig. 7, middle) is similar to the binary vanadia–titania aerogel. Small spheres aggregated into patches are discernible, giving rise to a relatively compact surface. Other particles appear to consist of small spheres in more open, sponge-type agglomerates.

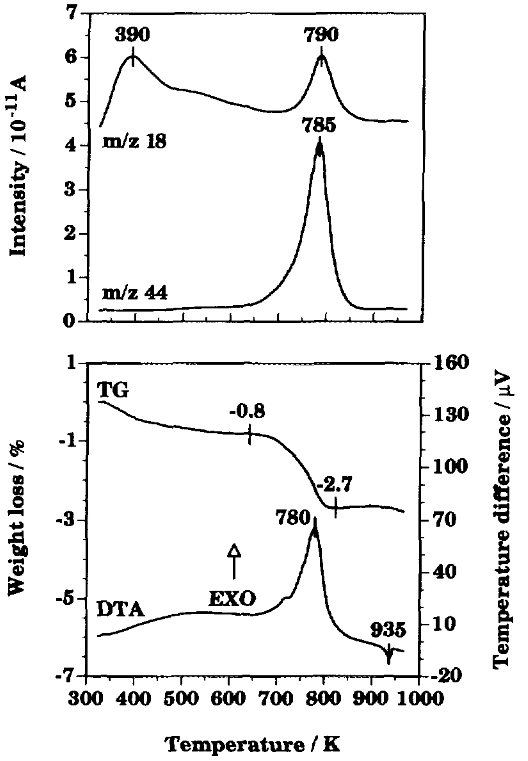

FIG. 6. Thermoanalytical investigation of xerogel V20Nb6*X* calcined at 673 K. Bottom, TG and DTA curves; top, ion intensities of $m/z(CO_2^+)$ = 44 (CO_2) and $m/z(H_2O^+)$ = 18 (water). Heating rate, 10 K min^{-1}; air flow, 25 ml min^{-1}.

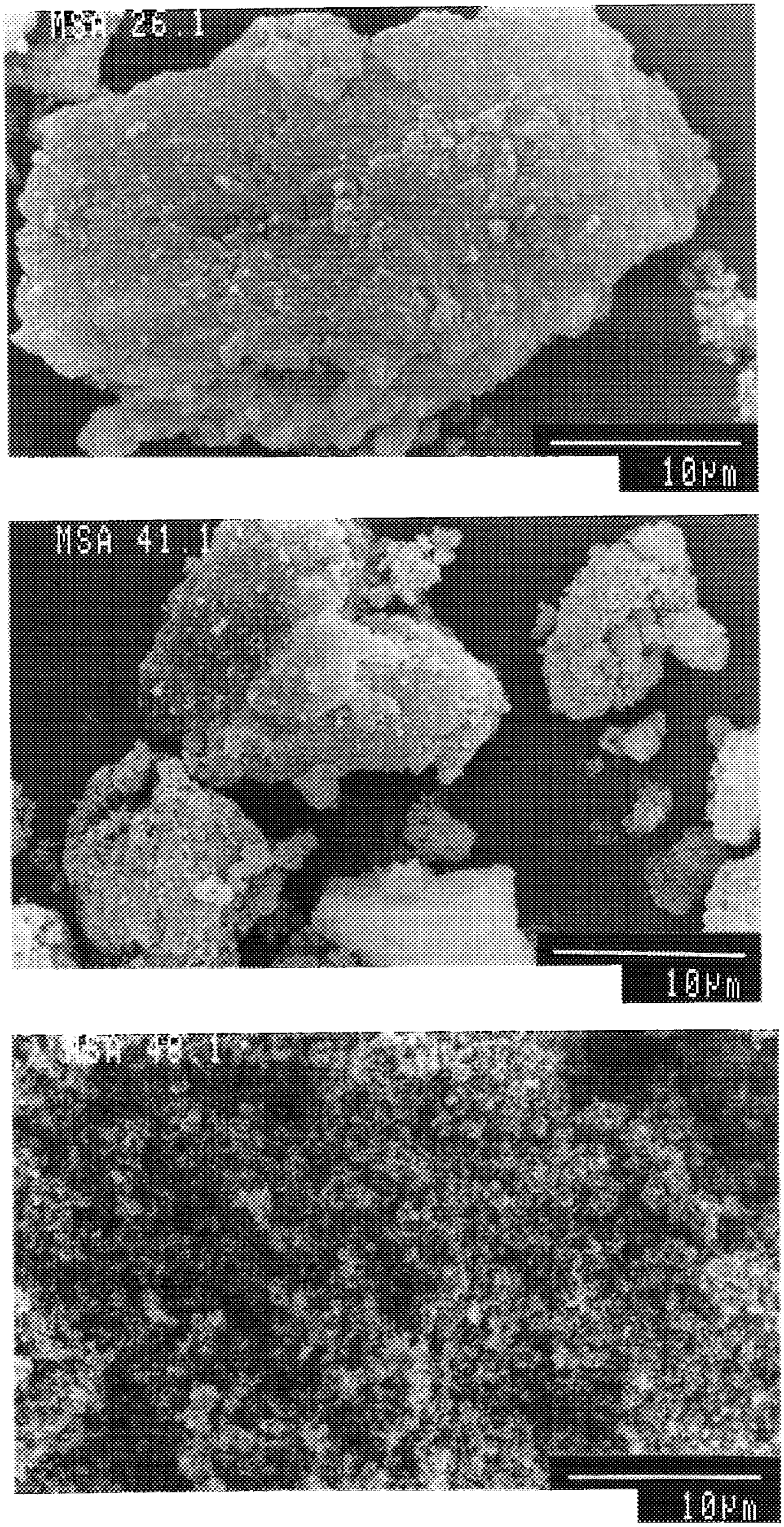

FIG. 7. SEM images of V20*NP*10 (top), V20Nb6 (middle), and Nb6 (bottom), all calcined at 573 K in air. Catalyst designations are explained under Experimental.

The morphology of ternary xerogels V20Nb6*X* calcined at different temperatures is shown in Fig. 8. Note that the particles are substantially larger than those of the aerogels. Although the micrographs of Figs. 7 and 8 were recorded at the same magnification, only a fraction of the respective particle surface is imaged in Fig. 8.

In detail, the surface of the xerogel calcined at 573 K (Fig. 8a) consists of stacked, disk-like terraces with sharp edges. Finer particles are scattered on top of the compact surface of the larger plates; no finer details of the surface structure of the latter can be discerned from the micrograph. Calcination at 673 K did not result in qualitative alterations of the appearance, although the individual plates have grown apparently both in lateral extent and thickness; again no fine structure is seen. After treatment at the highest calcination temperature (773 K), the major portion of the catalyst surface exhibits a glass-like smoothness. It is covered with small needles which are protruding from the bulk into different directions. When observed at higher magnification (Fig. 8d), the needles exhibit prismatic morphologies.

Vibrational spectroscopy. Raman spectra of the ternary aerogels with different niobia contents (2–6 wt%) are compared with the binary aerogels Nb6 and V20*NP*10 in Fig. 9. In the spectrum of the niobia–titania aerogel (bottom trace), the only features resolved are the vibrations of the anatase modification of TiO_2 at 635, 512, and 400 cm^{-1}. The presence of a major amorphous fraction of material is indicated by the high inelastic scattering background; absence of niobia-related features may be partly due to the low weight fraction of the latter component. With the binary vanadia–titania sample (second trace from bottom), the anatase fraction of the titania matrix is discerned by the vibration at 635 cm^{-1}. In addition, broad unstructured bands at ca. 520 and 800 cm^{-1}, and a weaker signal at ca. 400 cm^{-1} are detected. These spectral regions are characteristic for the skeletal stretching and deformational modes of both vanadia clusters and the two relevant titania modifications. The absence of sharp bands suggests that the vanadia fraction of the material consists of mainly ill-structured VO_x domains, but precludes any specific assignments. The spectra of the niobia-containing ternary aerogels V20Nb2, V20Nb4, and V20Nb6 (top three traces) are similar among each other, but different from those of the binary aerogels. Independent of the amount of added niobia, a broad and unstructured band with maximum at 420 cm^{-1} is dominating the spectrum. This feature is assigned to symmetric stretching modes and various deformational modes of oligomeric VO_x clusters, up to tri- and tetrameric species (2). The corresponding asymmetric stretching vibrations give rise to a weaker band at ca. 780 cm^{-1}. Vibrations of the anatase modification of TiO_2, the presence of which was deduced from X-ray diffraction, are not detected except for a weak band at 633 cm^{-1}. The surface appears to be covered with small VO_x clusters, such that the exciting laser does not penetrate to excite the vibrations of the anatase material underneath.

The influence of the niobia loading on the FTIR spectra is shown in Fig. 10. In the hydroxyl stretching region (left side), a pronounced difference is recognized between the binary niobia–titania aerogel and the vanadia-containing catalysts. In the spectrum of the Nb6 sample (bottom trace), strong absorptions are detected at 3729 and 3715 cm^{-1}. In the region below 3700 cm^{-1}, intense absorptions are observed at 3689 and 3677 cm^{-1} with a shoulder at 3636 cm^{-1}. Referring to the assignment of the hydroxyl stretching vibrations detected for a titania aerogel (2), the bands above 3700 cm^{-1} are attributed to basic hydroxyl groups (39); the intensity of these features has increased as compared to the pure titania aerogel (2). One concludes that any reaction between the niobia alkoxide precursor and the redispersed titania matrix appears to involve only the acidic OH groups of the titania surface. In the binary 20 wt% vanadia–titania aerogel (trace b), a broad band with a maximum at 3655 cm^{-1} and an asymmetry toward lower wavenumbers is observed; no bands above 3690 cm^{-1} are detected. In the niobia-doped ctalysts (top three traces), the Ti–OH absorption at 3677 cm^{-1} broadens the above-mentioned band toward higher frequencies. The maximum of the composite absorption is again found at 3655 cm^{-1}, and is assigned to V–OH groups at the surface (40–42).

The overtone region of the vanadyl stretching vibrations displayed in the right half of Fig. 10 exhibits an absorption maximum at 2050 cm^{-1} for the ternary aerogels, which remains unchanged as the niobia loading is varied between 2 and 6 wt%. We note, however, that the $2\nu(V{=}O)$ vibration of the binary vanadia–titania aerogel is detected at the significantly lower wave number of 2035 cm^{-1}. For supported vanadia/titania catalysts, the latter spectral position has been attributed to two-dimensional patches with a square pyramidal coordination of the vanadia centers (43, 44). The shift of the $2\nu(V{=}O)$ to higher wavenumbers upon niobia addition indicates a stronger interaction of the dispersed VO_x species with the titania matrix.

The influence of the calcination temperature on the surface structure of the aerogel V20Nb6 is monitored in the Raman spectra of Fig. 11. After calcination at 673 K the spectrum is largely unchanged as compared to the one of the material calcined at 573 K. Broad bands at ca. 460 and 800 cm^{-1} assigned to symmetric and asymmetric stretching modes of small vanadia clusters are dominating the spectrum. A small broad feature at 635 cm^{-1} is indicative of the anatase domains in the titania matrix. No specific assignments to NbO_x species can be made from these Raman spectra. The stretching modes of crystalline and supported niobium oxide are expected in the region be-

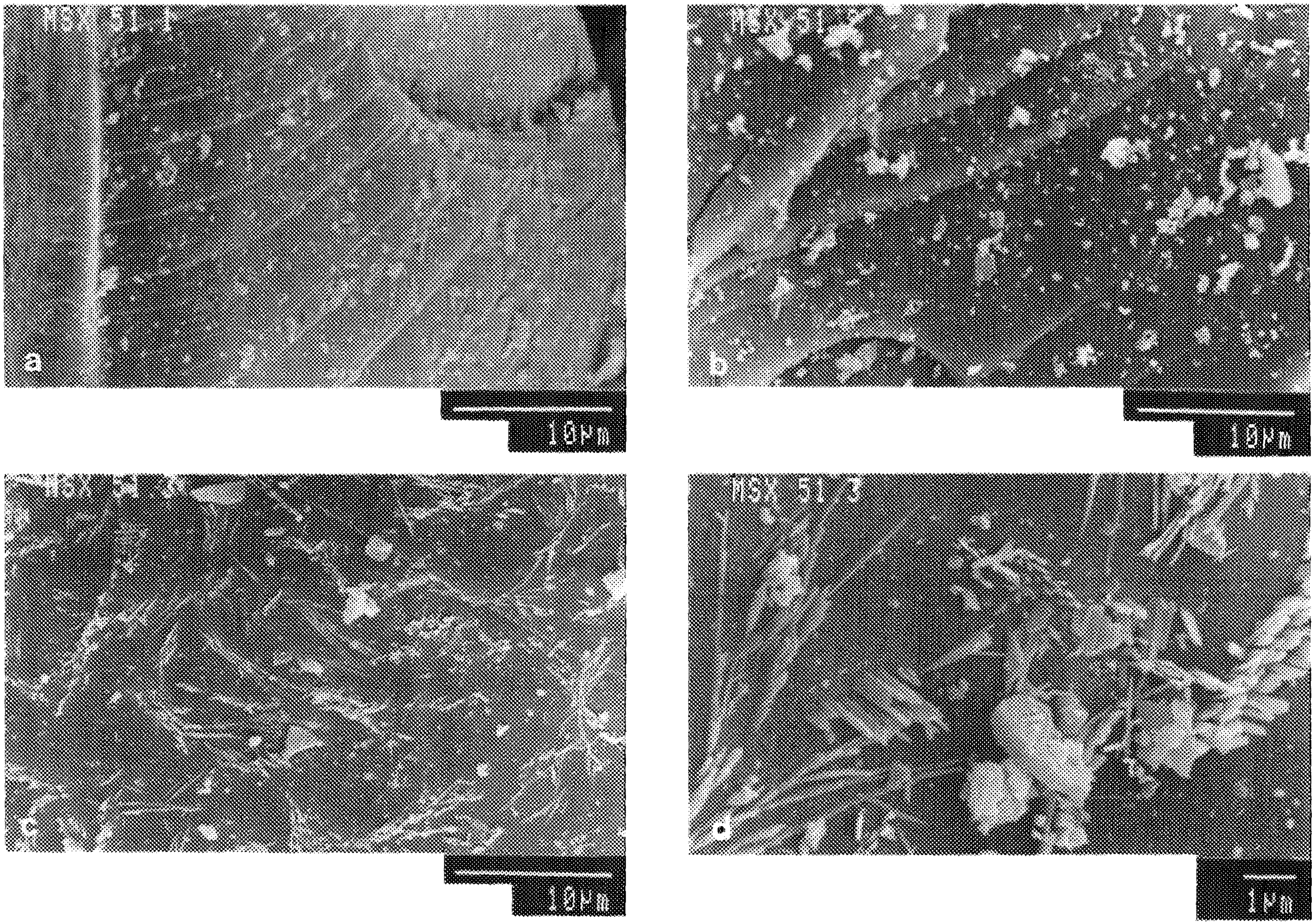

FIG. 8. SEM images of xerogel V20Nb6*X* calcined in air at different temperatures. (a) 573 K, (b) 673 K, (c, d) 773 K.

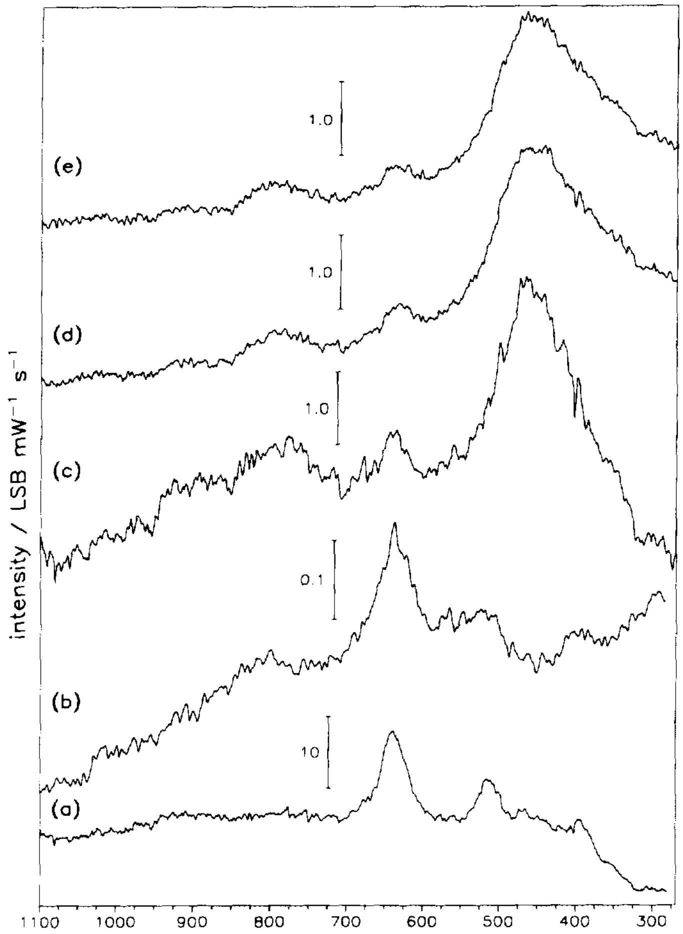

FIG. 9. Raman spectra of the niobia-loading series. (a) Nb6, (b) V20*NP*10, (c) V20Nb2, (d) V20Nb4, (e) V20Nb6. All calcined at 573 K in air. Designations of catalysts are explained under Experimental.

tween 300 and 550 cm^{-1} (45), where only a broad band is observed with the samples calcined at 573 and 623 K. Studies on impregnated catalyst systems have shown that the niobyl stretching vibration ν(Nb=O) of supported niobia is detected in the region between 880 and 990 cm^{-1} (46). For a dehydrated 7 wt% niobia/titania catalyst, Jehng and Wachs (46) have reported bands between 935 and 985 cm^{-1}. The frequency of the niobyl stretching vibration depends strongly on both the bond distances and on interactions with the support (45–47). This situation is analogous to the one known for supported vanadia catalysts, for which the ν(V=O) mode is recorded in the same spectral region. Therefore, a discrimination between ν(V=O) and ν(Nb=O) is not possible in the Raman spectra of the ternary samples. Calcination at 723 K resulted in the generation of three-dimensional VO_x aggregates at the surface. In the top spectrum of Fig. 11, this is apparent from the observation of peaks at 275 and 401 cm^{-1} (δ_s and δ_{as}(V=O)), at 629 cm^{-1} ($\nu_{as}(V_2O)$) and at 990 cm^{-1} (ν(V=O)), which are well known from the spectrum of crystalline V_2O_5 (48). The detected broadening of the peaks indicates imperfections of the V_2O_5 domains, or else superimposed contributions from vibrations of small VO_x clusters. In addition, a weak but significant band at 1010 to 1030 cm^{-1} shows the existence of two-dimensionally aggregated vanadia patches, which have been extensively characterized for supported catalyst (43, 49, 50). For higher Nb_2O_5 contents up to 20 wt%, Pittman and Bell (47) have reported the growth of islands of bulk-like Nb_2O_5 on titania surfaces.

Raman spectra of differently calcined xerogels are quite different in appearance (Fig. 12). For the material calcined at 573 K (bottom trace), a broad unstructured band between 450–700 cm^{-1} is indicative of an amorphous network, in agreement with the results of X-ray diffraction analysis. Calcination at 673 K resulted in broad bands with maxima at ca. 400 and 520 cm^{-1}, and a dominating intense band at 632 cm^{-1}. These vibrations are characteristic for anatase domains of the titania matrix, and appear to be broadened by superposition of vibrations of small VO_x clusters up to tetrameric species (2). In addition, two-dimensionally connected patches of dispersed vanadia are identified from a weak band at 1028 cm^{-1} and a shoulder at 284 cm^{-1} (51–54). The spectrum of the xerogel calcined at 773 K is characterized by vibrations of crystalline V_2O_5 at 993, 405, and 285 cm^{-1}. Other skeletal vibrations at 483, 530, and 703 cm^{-1} are weaker and significantly broadened. The presence of the rutile modification of TiO_2 is deduced from the observation of a band at ca. 610 cm^{-1} and a shoulder at 440 cm^{-1}. The superimposed vibrations of anatase give rise to a broadening of these bands.

FTIR spectra of the xerogel catalysts are shown in Fig. 13. After calcination at 573 K, a weak and broad absorption extending from 2800 to 3625 cm^{-1} is seen if the spectrum is plotted on an expanded scale. This band is usually attributed to physisorbed water. Recalling that the sample was heated in situ to 473 K for 20 min under a flow of dry oxygen, this observation suggests that water and/or methanol have been entrapped in the pores of the amorphous network. Strong absorptions in the spectral range between 1200 and 1800 cm^{-1} are assigned to C–C stretching vibrations of organic residues, for which a high fraction (7.8 wt%) was determined (see thermoanalytical results above). The corresponding C–H stretching vibrations are seen at 2800–3000 cm^{-1}. The intense sharp peak at 2348 cm^{-1} has been attributed to isolated OH groups on the surface of ZrO_2 supports (55), with extremely strong bridging hydrogen bonds to the oxidic surrounding. The FTIR absorption of anatase, at 980 cm^{-1}, is detected as a weak shoulder besides the maximum at 1014 cm^{-1}, assigned to the V=O stretching vibration. Upon increasing the calcination temperature to 673 K, the absorption of

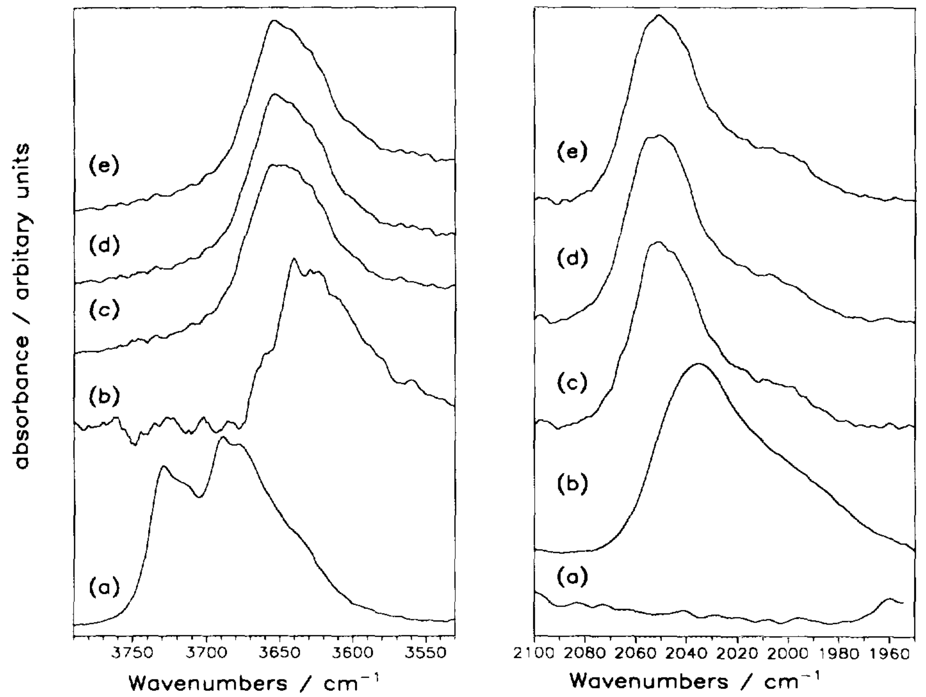

FIG. 10. FTIR spectra of the niobia-loading series. Left, OH stretching region; right, $2\nu(V{=}O)$ overtone region. (a) Nb6, (b) V20*NP*10, (c) V20Nb2, (d) V20Nb4, (e) V20Nb6; all calcined at 573 K in air.

the enclosed organic residues decreases drastically, and the band from physisorbed water disappears. The absorption of titania at 980 cm^{-1} has increased in intensity, whereas the maximum of the absorption at 1015 cm^{-1} is broadened. The $2\nu(V{=}O)$ overtone region at 1950 to 2100 cm^{-1} (inset) shows a band at 2044 cm^{-1}, which has been assigned to two-dimensional patches of dispersed vanadia on the titania surface. After calcination at 773 K (top trace of Fig. 13), the absorptions of organic residues are no longer detected. The weak vibration at 2348 cm^{-1} is the only signal assigned to remnant hydroxyl groups in the spectrum. The anatase band at 980 cm^{-1} has increased in intensity, and is dominating the spectrum. The overtone of the vanadyl absorption shows maxima at 2020 and 1980 cm^{-1}, which are well known from the FTIR spectrum of crystalline V_2O_5 (56).

Selective Catalytic Reduction of NO by NH_3

The catalytic data are listed in Table 3. Note that the specific activities at 423 K were compared on the basis of turnover frequencies TOF in [(mol NO) (mol V)$^{-1}$ s^{-1}], reaction rates per BET surface area [(mol NO) m^{-2} s^{-1}] as well as reaction rates per gram catalyst [(mol NO) $(g_{cat})^{-1}$ s^{-1}]. TOF values were based on the assumption that all vanadium species are accessible for the reactant gases. The appropriate amount of vanadium was calculated from the designed loading, as noted in the experimental section. With regard to the intrinsic contribution of the niobia phase, it was previously reported (19) that below 573 K niobia–titania does not reveal any significant SCR activity, mainly due to its poor redox functionality. Further evidence for this behavior will be given below. Altogether, reaction rates per overall vanadium TOF represent "conservative" estimates of intrinsic (TOF) values. It is obvious that the S_{BET} is a nonselective measure of the active surface area (surface sites are not selectively titrated). Yet if we assume that the compositional and chemical effects on the active sites are displayed by the TOF values, then S_{BET}-related reaction rates should be reasonable estimates of the vanadia dispersity. As a measure of the overall activity, the temperature necessary for 50% NO conversion ($T_{50\%}$) under standard conditions is quoted.

The NO and NH_3 conversion plots of the niobia-loading series depicted in Fig. 14 indicate that the aerogel catalysts with 20 wt% V_2O_5 and 0, 2, 4, or 6 wt% Nb_2O_5 exhibited a virtually identical overall activity after calcination at 573 K. This behavior is further supported by the tmperatures necessary for 50% NO conversion listed in Table 3, which did not change significantly with increasing niobia loading. With Nb6, the binary niobia–titania aerogel with 6 wt% Nb_2O_5, only negligible activity was measured up to 558 K (19). The invariable catalytic behavior of the ternary aerogel catalysts calcined at 573 K is further illustrated

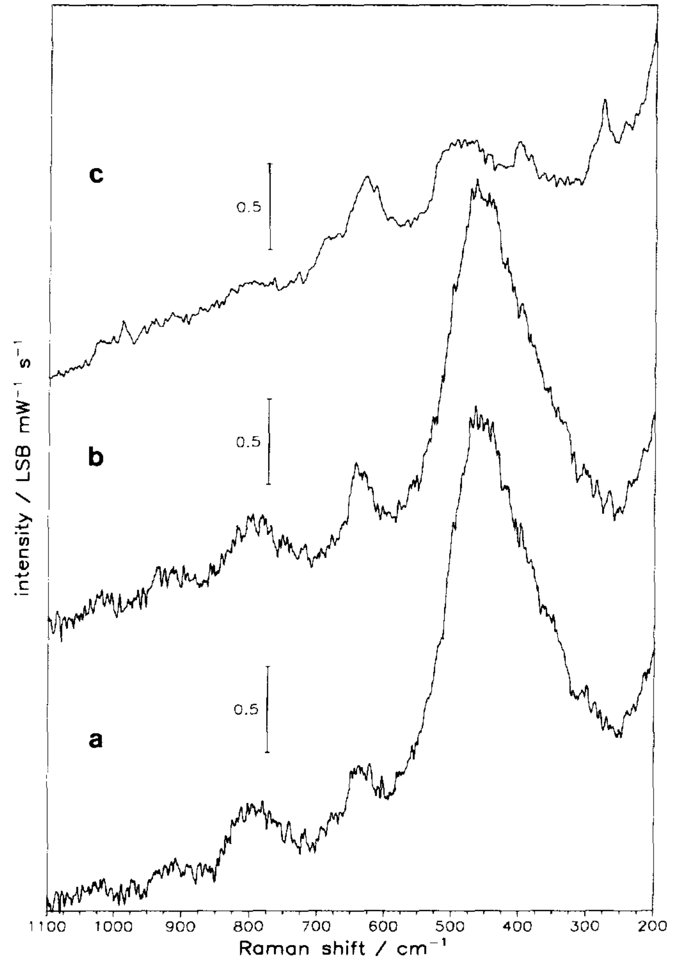

FIG. 11. Raman spectra of aerogel V20Nb6 calcined in air at different temperatures. (a) 573 K, (b) 673 K, (c) 723 K.

by the virtually identical kinetic results presented in Table 3. These data are again comparable to the corresponding reaction rates of the binary vanadia–titania aerogel catalyst V20*NP*10 taken from Ref. (1).

NH_3 conversions were generally up to 5% higher than NO conversions at higher temperatures due to a small loss to direct oxidation. This oxidation generally occurred at ca. 470 K and seemed to keep a constant level up to 558 K (the highest temperature of integral reactor testing). The N_2O production was also minimal and became apparent beyond ca. 510 K. It reached concentration levels of several vppm, which were close to the mass spectrometric detection limit of N_2O.

The influence of the calcination temperature on the catalytic performance of the aerogel series V20Nb6 calcined at 573, 673, and 723 K is represented by the corresponding Arrhenius plots in Fig. 15 and the data listed in Table 3. The calcination at 673 and 723 K resulted in a significant increase of TOF, reaction rate per S_{BET}, and reaction rate per gram catalyst, while the apparent activation energies were the same considering the confidence limits (Table 3). This catalytic behavior can be explained by temperature induced migration and agglomeration (see vibrational spectroscopy studies above, Fig. 11), which led to larger accessibility and possibly higher intrinsic activity (57, 58) of the vanadia species. Another beneficial effect of the calcination at 673–723 K might be the partial removal of organic contaminants from the active surface fraction. A similar behavior was found for the binary vanadia–titania aerogels reported in Part I (1). For comparison, the corresponding specific reaction rates as well as the overall activity data of the binary aerogel catalyst V20*STA*673, calcined at 673 K and quoted from Ref. (1), were added to Table 3.

The effect of calcination was even much more pronounced with the xerogel V20Nb6*X*. As mentioned

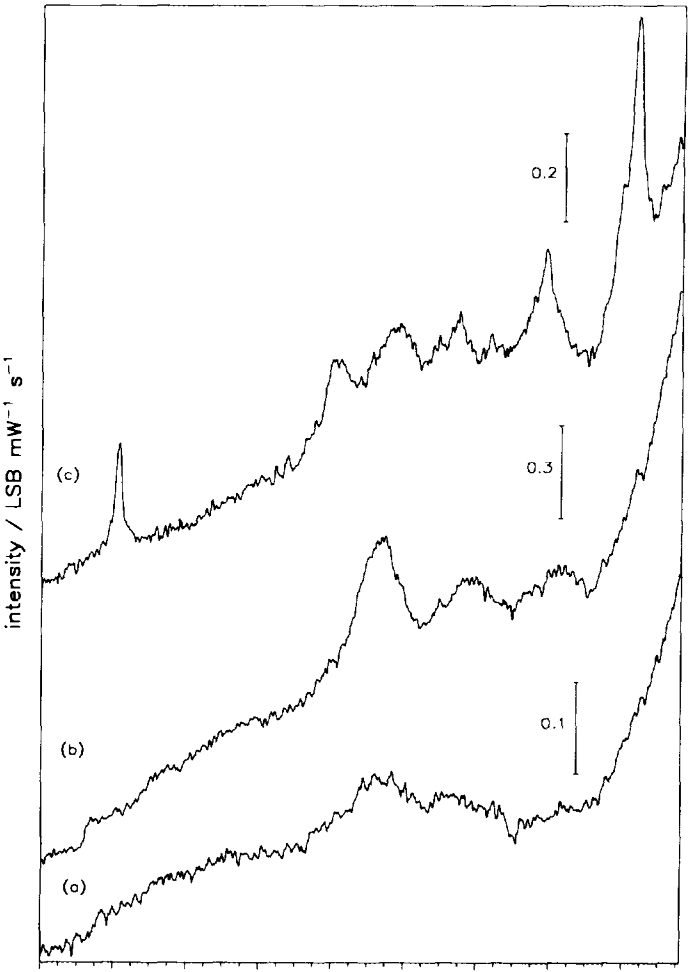

FIG. 12. Raman spectra of xerogel V20Nb6*X* calcined in air at different temperatures. (a) 573 K, (b) 673 K, (c) 773 K.

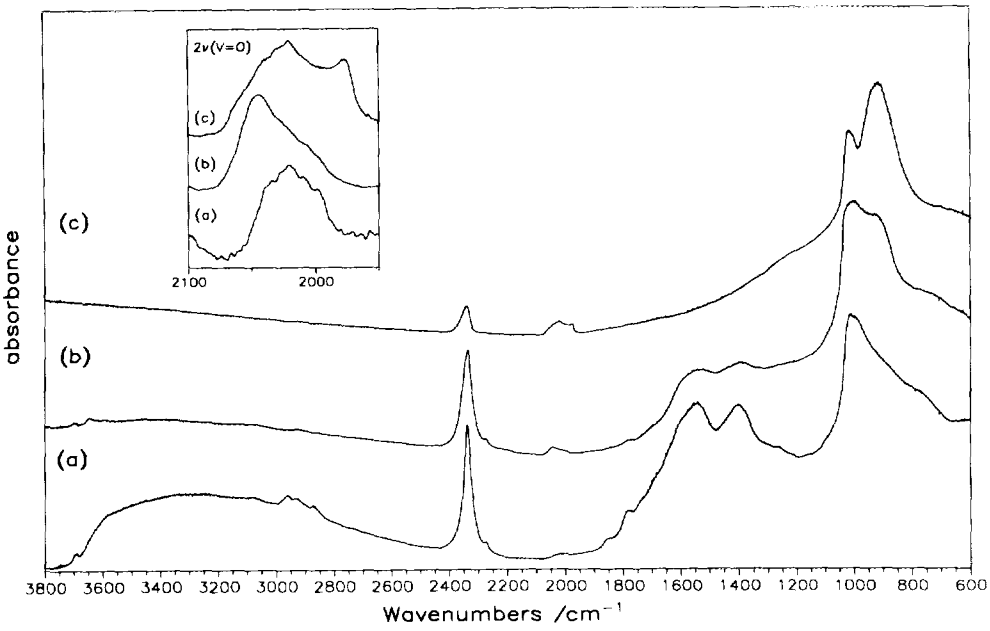

FIG. 13. FTIR spectra of xerogel V20Nb6*X* calcined in air at different temperatures. (a) 573 K, (b) 673 K, (c) 773 K. Inset: 2ν(V=O) overtone region.

above, the oxidative treatment at 573 K for 5 h did not suffice to free the pores from the organic contaminants. The internal xerogel surface remained virtually unaccessible (see thermoanalytical studies above). However, the calcination at 673 K opened the micro- to mesoporous xerogel structure for the reactant gases (Fig. 2) and thus removed part of the organic contaminants from the active surface fraction (Figs. 12 and 13). Despite the residual 1.7 wt% carbon left in the matrix, the ternary xerogel catalyst V20Nb6*X* calcined at 673 K exhibited the highest

TABLE 3

Selective Catalytic Reduction of NO by NH_3

Aerogel	Calcination (K)	'TOF'[a] × 10^4 (mol NO/mol V/s)	$r_s \times 10^9$ (mol NO/m^2/s)	$r_w \times 10^7$ (mol NO/g$_{cat}$/s)	E_a (kJ/mol)	$T_{50\%}$ (K)
V20*NP*10[b]	573	1.5	1.5	3.2	58	435
V20*STA*673[c]	673	1.7	2.1	3.6	60	429
Nb6	573	—	—	—	—	—
V20Nb2	573	1.4	1.5	3.0	59	436
V20Nb4	573	1.4	1.6	3.0	61	436
V20Nb6	573	1.4	1.6	3.0	62	436
V20Nb6	673	1.6	1.9	3.4	63	432
V20Nb6	723	1.8	3.5	3.9	62	427
V20Nb6*X*	673	2.3	4.3	5.0	55	387[d]

Note. The kinetic data measured at 423 K are represented as turnover frequency (TOF), reaction rate per BET surface area (r_s), reaction rate per gram catalyst (r_w), and apparent activation energy (E_a); results of integral reactor tests are represented as temperature required for 50% NO conversion under standard conditions.

[a] Reaction rate referred to the designed vanadium content (TOF) on the basis of the assumption that all vanadium species are accessible to the reactant gases.

[b] From Ref. (*1*): V20*NP*10 20 wt% V_2O_5; basic preparation procedure for this work.

[c] From Ref. (1): V20*STA*673 20 wt% V_2O_5, 178 m^2 g^{-1}; included for comparison with the V20Nb6 series, showing the effect of the calcination temperature without niobia.

[d] 112 mg$_{cat}$ (instead of 44 mg$_{cat}$ with the aerogel catalysts).

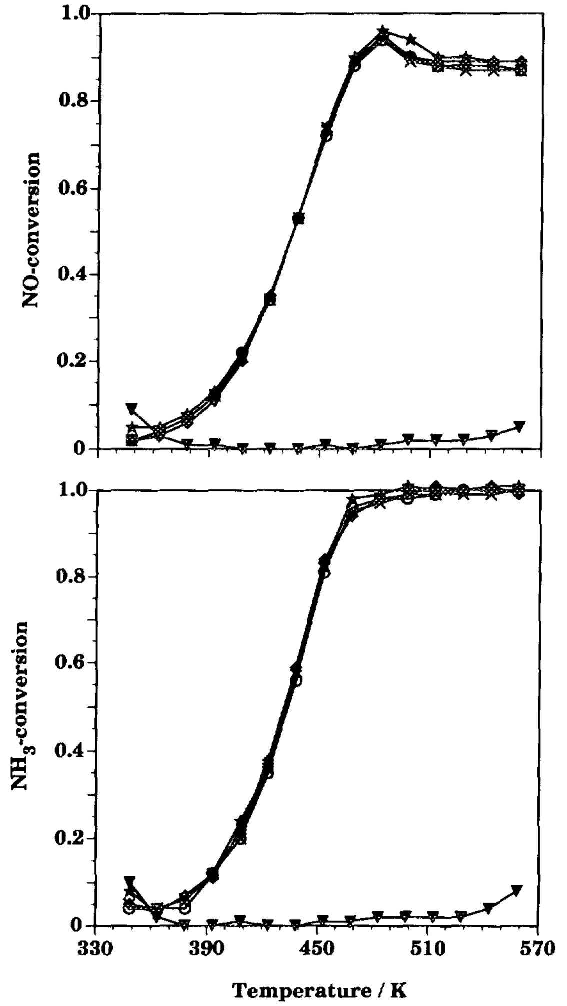

FIG. 14. SCR activities of niobia-doped vanadia–titania aerogels as a function of temperature. Top, NO conversion; bottom, NH_3 conversion. ▼, Nb6; ★, V20*NP*10; ⊙, V20Nb2; ×, V20Nb4; ◆, V20Nb6. All calcined in air at 573 K. Catalyst designations are explained under Experimental.

activity among all catalysts presented in this work (Fig. 15, Table 3).

DISCUSSION

Although the loading of Nb_2O_5 was varied from 0 to 6 wt%, both the textural and structural properties of the aerogel samples calcined at 573 K were almost not influenced (Table 2). Meso- to macroporous aerogels were obtained in all cases, with BET surface areas of ca. 200 $m^2 g^{-1}$. The aerogels contain anatase crystallites of ca. 7 nm mean size. The X-ray amorphous vanadia phase of the aerogels was only detectable by vibrational spectroscopy and is suggested to consist of ill-defined, small vanadia clusters uniformly spread throughout the titania matrix (Figs. 3 and 9). When compared to the binary vanadia–titania aerogels presented in Part I of these studies (1), the niobia addition did not affect the catalytic activity of the ternary aerogels (Fig. 14, Table 3). This catalytic behavior could be indicative of physical separation of the vanadia and niobia components. They are very likely to form isolated islands of clusters, which build up only a negligible interfacial area. Recall that niobia–titania does not reveal any significant activity below 573 K (Fig. 14). So considering the poor redox functionality of niobia (19), a promoting effect would probably only occur due to the formation of active sites at the interface.

The calcination of two portions of the ternary aerogel V20Nb6 with 6 wt% Nb_2O_5 at 673 and 723 K resulted in a controlled decrease of the BET surface area to 176 and 114 $m^2 g^{-1}$, respectively, preserving the meso- to macroporosity. The calcination at 723 K caused a slight growth of the anatase crystallites to 10 nm mean size. The vanadia as well as the niobia phase remained X-ray amorphous. However, the vibrational spectroscopy studies showed that the temperature-induced migration and/or agglomeration of the small vanadia clusters led to two-dimensionally connected patches and even three-dimensional multilayered structures (Fig. 11). This restructuring resulted in a significantly increased activity for SCR. The temperature-induced migration agglomeration of the vanadia component was ascertained previously with the binary aerogels reported in Part I (1) of this series. In contrast to those findings, the calcination at 723 K did not lead to crystallization and concomitant anatase-to-rutile transformation, which would have resulted in a

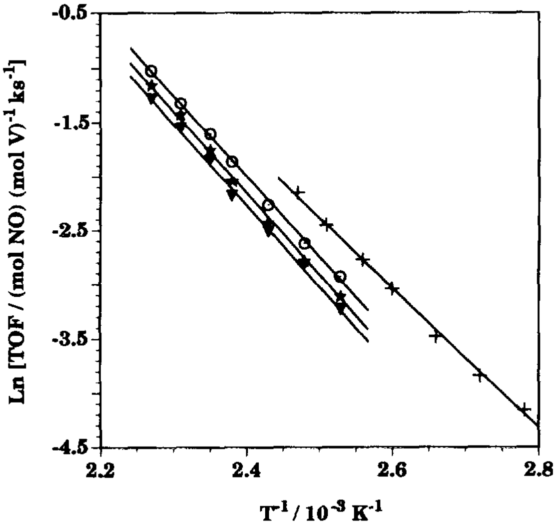

FIG. 15. Arrhenius plots of specific SCR rates measured over aerogel V20Nb6 calcined at different temperatures and xerogel V20Nb6*X* calcined at 673 K. ▼, V20Nb6, 573 K; ★, V20Nb6, 673 K; ⊙, V20Nb6, 723 K; +, V20Nb6*X*, 673 K.

major change of the textural properties. Consequently, it seems that up to 723 K niobia suppresses the crystallization of vanadia and thus favors further migration–agglomeration with a concomitant buildup of the most active vanadia sites, described as two-dimensional disordered arrays of octahedrally bound vanadium oxo oligomers (57, 58), and/or larger accessibility.

For TiO_2-supported niobia–vanadia, Wachs *et al.* (59) reported that two-dimensional surface overlayers of niobia interact strongly with the titania surface and are stable up to high calcination temperatures (<1223 K). This interaction results in retardation of solid-state transformations, i.e., phase transformation of anatase to rutile, formation of crystalline Nb_2O_5 or Nb–O–Ti phases, and a loss in surface area of TiO_2 supports. Moreover, surface niobia was found to stabilize "metastable" surface overlayers of vanadia in mixed vanadia–niobia/TiO_2 solids. This property of two-dimensional surface niobia was utilized in vanadia–niobia/TiO_2 catalysts for control of NO_x emission from stationary sources (60). These ternary catalysts were effective in a wide temperature range with little SO_2 oxidation and exhibited NO conversions of 85–95% at 523–723 K and a space velocity of 15000 h^{-1}. Bearing in mind that a similar rise in activity is observed for the binary vanadia–titania aerogel V20*STA*673 upon calcination at 673 K (1) (Table 3), it is unlikely that additional beneficial effects of the calcination, especially at 723 K, can be attributed to the formation of active vanadia–niobia interfaces.

The comparison between conventionally and supercritically dried samples (xerogel versus aerogel) reveals distinct morphological, structural, and chemical differences. In contrast to the corresponding aerogel V20Nb6, the xerogel V20Nb6*X* remained X-ray amorphous up to 573 K and crystallized to anatase as well as monoclinic TiO_2 during calcination at 673 K (Fig. 4, Table 2). The large amount of organic residues in the raw xerogel (16.4 wt% carbon) revealed a marked thermal resistance toward calcination up to 673 K (Fig. 6), based on the microporous structure of the xerogel (Fig. 2). Even after calcination at 673 K for 5 h, 1.7 wt% carbon persisted in the xerogel sample. However, this temperature was high enough to make most of the internal surface area accessible (Fig. 2, Table 2) and to remove a part of the organic contaminants from the active surface fraction. When the Raman spectrum of this sample is compared to that of the amorphous xerogel sample calcined at 573 K, this picture of the calcination process is further supported by the appearance of two-dimensionally connected patches and small clusters of vanadia after calcination at 673 K (Fig. 12). A further increase of the calcination temperature to 773 K led, however, to a loss of the microporosity and consequently also of the BET surface area due to crystallization of V_2O_5 and concomitant, partial anatase-to-rutile transformation (1, 36–38). The highly dispersed vanadia phase of the xerogel catalyst V20Nb6*X*, calcined at 673 K and with two-dimensionally connected vanadia patches besides small vanadium oxo clusters, as well as the removal of the organic residues from the porous xerogel, both combined with the retention of the remarkable BET surface area (117 $m^2\,g^{-1}$), resulted in the highest SCR activity among all ternary catalysts tested (Table 3). The reaction rates of this material, referred to the vanadium content or related to the BET surface area, are similar to that of the binary vanadia–titania aerogel with 30 wt% V_2O_5, as presented in Ref. (1). However, due to the lower nominal V_2O_5 loading of 20 wt%, the reaction rate per gram catalyst amounts to 60% of the rate measured for the binary aerogel catalyst calcined at 573 K and loaded with 30 wt% V_2O_5 (1). The higher activity of the xerogel compared to the aerogels might be rationalized on grounds of the lower BET surface area, which usually provides a rough estimate of the amount of vanadia needed to form active two-dimensional disordered arrays of octahedrally bound vanadium oxo oligomers. These structural units have been suggested to be the most active sites in highly dispersed multiply grafted vanadia on titania SCR catalysts (57, 58). When compared to the BET surface area (117 $m^2\,g^{-1}$) and to the composition of the V20Nb6*X* xerogel calcined at 673 K, the aerogel V20Nb6 calcined at 723 K possesses a comparable BET surface area of 114 $m^2\,g^{-1}$ (Table 2) and the same composition. However, the SCR activity of the aerogel portion V20Nb6 calcined at 723 K is significantly lower than that of the xerogel V20Nb6*X* calcined at 673 K. This phenomenon merits further investigation.

CONCLUSIONS

The addition of different amounts of niobia affected neither the textural nor the structural properties of the niobia-containing aerogels calcined at temperatures ≤673 K. A significant decrease of the BET surface area and increase of the mean anatase crystallite size occurred during calcination at 723 K. Both the vanadia and niobia phase remained X-ray amorphous. However, the structural evolution as well as the dispersion of the vanadia component are strongly influenced by the calcination temperature. The calcination at 673 and 723 K caused migration of the vanadia phase, which predominantly consisted of ill-defined small vanadium oxo clusters, and buildup of two-dimensionally connected patches as well as three-dimensional multilayered structures (agglomeration). This restructuring resulted in a significant increase of the activity for SCR of NO by NH_3. A comparison between a conventionally dried xerogel and supercritically dried aerogel, both with 20 wt% nominal V_2O_5 and 6 wt% nominal Nb_2O_5, revealed distinct morphological, structural, and chemical differences. The raw xerogel contains much more organic residues, is X-ray amorphous and possesses a microporous structure. The xerogel had to be calcined at 673 K to liberate the internal structure from the organic contaminants, which made the active surface fraction accessible for the reactant gases. The vanadia phase consists again of small vanadium oxo clusters together with larger two-dimensional patches. The xerogel catalyst calcined at 673 K revealed the highest activity among the catalysts tested in this work.

ACKNOWLEDGMENT

Financial support by the Nationaler Energie-Forschungs-Fonds (NEFF 569) is gratefully acknowledged.

REFERENCES

1. Schneider, M., Maciejewski, M., Tschudin, S., Wokaun, A., and Baiker, A., *J. Catal.* **149,** 326 (1994).
2. Scharf, U., Schneider, M., Baiker, A., and Wokaun, A., *J. Catal.* **149,** 344 (1994).
3. Baiker, A., Dollenmeier, P., Glinski, M., and Reller, A., *Appl. Catal.* **35,** 351 (1987).
4. Bosch, H., and Janssen, F., *Catal. Today* **2,** 1 (1987).
5. Inomata, M., Miyamoto, A., and Murakami, Y., *J. Catal.* **62,** 140 (1980).
6. Janssen, F. J. J. G., Van den Kerkhof, F. M. G., Bosch, H., and Ross, J. R. H., *J. Phys. Chem.* **91,** 6633 (1987).
7. Chen, J. P., and Yang, R. T., *J. Catal.* **125,** 411 (1990).
8. Chen, J. P., and Yang, R. T., *Appl. Catal. A* **80,** 135 (1992).
9. Topsøe, N.-Y., Slabiak, T., Clausen, S. B., Srnak, T. Z., and Dumesic, J. A., *J. Catal.* **134,** 742 (1992).
10. Srnak, T. Z., Dumesic, J. A., Clausen, B. S., Törnqvist, E., and Topsøe, N.-Y., *J. Catal.* **135,** 246 (1992).
11. Ramis, G., Busca, G., Bregani, F., and Forzatti, P., *Appl. Catal.* **64,** 259 (1990).
12. Schneider, H., Tschudin, S., Schneider, M., Wokaun, A., and Baiker, A., *J. Catal.* **147,** 5 (1994).
13. Tanabe, K., *Catal. Today* **8,** 1 (1990).
14. Tanabe, K., *Catal. Today* **16,** 289 (1993).
15. Maurer, S. M., and Ko, E. I., *J. Catal.* **135,** 125 (1992).
16. Maurer, S. M., and Ko, E. I., *Catal. Lett.* **12,** 231 (1992).
17. Maurer, S. M., Ng, D., and Ko, E. I., *Catal. Today* **16,** 319 (1993).
18. Datka, J., Turek, A. M., Jehng, J.-M., and Wachs, I. E., *J. Catal.* **135,** 186 (1992).
19. Okazaki, S., and Okuyama, T., *Bull. Chem. Soc. Jpn.* **56,** 2159 (1983).
20. Brinker, C. J., and Scherer, G. W., "Sol–Gel Science—the Physics and Chemistry of Sol—Gel Processing." Academic Press, San Diego, 1990.
21. Scherer, G. W., *J. Am. Ceram. Soc.* **73,** 3 (1990).
22. Pajonk, G. M., *Appl. Catal.* **72,** 217 (1991).
23. Ko, E. I., *Chemtech* **23(4),** 31 (1993).
24. Schneider, M., and Baiker, A., *in* "Encyclopedia of Advanced Materials" (D. Bloor, R. J. Brook, M. C. Flemings, and S. Mahajan, Eds.), Vol. 1. Pergamon, Oxford, 1994.
25. Thermodynamics Research Center The Texas A&M University System, *in* "TRC Thermodynamic Tables—Non-Hydrocarbons," Vol. IV, p. i-5000. College Station, 1992.
26. Barrett, E. P., Joyner, L. G., and Halenda, P. P., *J. Am. Chem. Soc.* **73,** 373 (1951).
27. Sing, K. S. W., Everett, D. H., Haul, R. A. W., Moscou, L., Pierotti, R. A., Rouquérol, J., and Siemieniewska, T., *Pure Appl. Chem.* **57,** 603 (1985).
28. Broekoff, J. C. P., *in* "Preparation of Heterogeneous Catalysts II" (B. Delmon, P. Grange, P. Jacobs, and G. Poncelet, Eds.), Vol. 3, p. 663. *Stud. Surf. Sci. Catal.*, Elsevier, Amsterdam, 1979.
29. Harkins, W. D., and Jura, G., *J. Chem. Phys.* **11,** 431 (1943).
30. Klug, H. P., and Alexander, L. E., "X-Ray Diffraction Procedures for Polycrystalline and Amorphous Materials." J. Wiley, New York, 1974.
31. JCPDS Mineral Powder Diffraction Data File, 21-1272, Park Lane, Pennsylvania.
32. JCPDS Mineral Powder Diffraction Data File, 21-1276, Park Lane, Pennsylvania.
33. JCPDS Mineral Powder Diffraction Data File, 35-0088, Park Lane, Pennsylvania.
34. Meier, M., Carron, K. T., Fluhr, W., and Wokaun, A., *Appl. Spectrosc.* **17,** 4 (1986).
35. JCPDS Mineral Powder Diffraction Data File, 9-0387, Park Lane, Pennsylvania.
36. Bond, G. C., Sárkány, A. J., and Parfitt, G. D., *J. Catal.* **57,** 476 (1979).
37. Véjux, A., and Courtine, P., *J. Solid State Chem.* **23,** 93 (1978).
38. Depero, L. E., Bonzi, P., Zocchi, M., Casale, C., and De Michele, G., *J. Mater. Res.* **8,** 2709 (1993).
39. van Veen, J. A. R., Veltmaat, F. T. G., and Jonkers, G., *J. Chem. Soc. Chem. Comm.*, 1656 (1985).
40. Hanke, W., Heise, K., Jerschkewitz, H. G., Lischke, G., Oehlmann, G., and Barlitz, B., *Z. Allg. Anorg. Chem.* **438,** 176 (1978).
41. Rajadhyaksha, R. A., and Knözinger, H., *Appl. Catal.* **51,** 81 (1989).
42. Leyrer, J., Mey, D., and Knözinger, H., *J. Catal.* **24,** 349 (1990).
43. Handy, B. E., Baiker, A., Schraml-Marth, M., and Wokaun, A., *J. Catal.* **133,** 1 (1992).
44. Jehng, J.-M., and Wachs, I. E., *Chem. Mater.* **3,** 100 (1991).
45. Jehng, J.-M., and Wachs, I. E., *J. Mol. Catal.* **67,** 369 (1991).
46. Jehng, J.-M., and Wachs, I. E., *J. Phys. Chem.* **95,** 7373 (1991).
47. Pittmann, R. M., and Bell, A. T., *J. Chem. Phys.* **97,** 12178 (1994); Pittmann, R. M., and Bell, A. T., *Catal. Lett.* **24,** 1 (1994).
48. Griffith, W. P., and Lesniak, P. J. B., *J. Chem. Soc. A*, 1066 (1969).
49. Machej, T., Haber, J., Turek, A. M., and Wachs, I. E., *Appl. Catal.* **70,** 115 (1991).
50. Deo, G., and Wachs, I. E., *J. Phys. Chem.* **95,** 5889 (1991).
51. Nag, N. K., Komandur, V. R., Chary, B., Rao, B. R., and Subrahmanyan, Y. S., *Appl. Catal.* **31,** 73 (1987).
52. Cristiani, C., Forzatti, P., and Busca, G., *J. Catal.* **116,** 586 (1989).
53. Scharf, U., Schraml-Marth, M., Wokaun, A., and Baiker, A., *J. Chem. Soc. Faraday Trans. 1* **87,** 587 (1992).
54. Schraml-Marth, M., Wokaun, A., Pohl, M., and Krauss, K. L., *J. Chem. Soc. Faraday Trans. 1* **87,** 2635 (1991).
55. Graetsch, H., Flörke, O. W., and Niehe, G., *Phys. Chem. Mineral* **12,** 300 (1985).
56. Cavani, F., Forzatti, E., Trifiró, F., and Busca, G., *J. Catal.* **106,** 2051 (1987).
57. Baiker, A., Handy, B., Nickl, J., Schraml-Marth, M., and Wokaun, A., *Catal. Lett.* **14,** 89 (1992).
58. Went, G. T., Leu, L.-J., Rosin, R. R., and Bell, A. T., *J. Catal.* **134,** 492 (1992).
59. Wachs, I. E., Jehng, J.-M., and Hardcastle, F. D., *Solid State Ionics* **32/33,** 904 (1989).
60. Yoshida, H., Morikawa, S., Takahashi, K., and Kurita, M., JP 82 48,342, March 19, 1982.